Korean J. Chem. Eng., 39(12), 3277-3285 (2022)
DOI: 10.1007/s11814-022-1226-9

pISSN: 0256-1115
eISSN: 1975-7220

Controllable synthesis of zinc oxide with ionic liquid and supramolecular gel as co-template for the degradation of organic dyes

Zhen Li*,‡, Lili Sun*,‡, Jie Zhang*, and Shaokun Tang*,,†**

*Key Laboratory for Green Chemical Technology of Ministry of Education, School of Chemical Engineering & Technology, Tianjin University, Tianjin 300072, China
**Collaborative Innovation Center of Chemical Science and Engineering (Tianjin), Tianjin University, Tianjin 300072, China
(*Received 11 March 2022 • Revised 27 June 2022 • Accepted 7 July 2022*)

Abstract−Zinc oxide was synthesized with ionic liquid tetramethylammonium glycine ($[N_{1111}][Gly]$) and supramolecular gel *N*-lauro-*L*-glutamic acid-di-n-butylamide (GP-1) as co-template by solvothermal method and characterized by X-ray diffraction (XRD), scanning electron microscopy (SEM), transmission electron microscopy (TEM) and UV-vis diffuse reflectance spectrometer. The effects of templating agent dosage and aging time on the morphology, mesoporous structure, and crystal phase of ZnO were investigated. The results demonstrate that the ionic liquid $[N_{1111}][Gly]$ and GP-1 organogel synergistically control the growth orientation of the crystal, and the morphology of ZnO varies with the templating agent dosage and aging time. The as-synthesized samples were applied in the catalytic degradation of Congo red under simulated solar light irradiation. In particular, the synthesized sample (MZ-3-8) with nanosheets morphology exhibited the best catalytic performance with a degradation rate up to 98% for 90 min, clearly superior to commercial ZnO and P-25. Furthermore, the catalyst can be cycled at least eight times with little loss of photocatalytic activity.

Keywords: Co-template, Ionic Liquid, Supramolecular Gel, Zinc Oxide, Photocatalysis

INTRODUCTION

Dye wastewater is one of the leading industrial discharge wastewaters, mainly containing refractory organic matters such as dyes and dye intermediates. Although dyes are widely used in medicine, food, and cosmetics, if not treated after discharge, they will lead to severe environmental problems due to their toxic and biorefractory properties [1]. A variety of techniques currently have been investigated for dyes removal, including adsorption [2], photocatalytic degradation [3], coagulation [4], and oxidation [5]. Among these methods, semiconductor-mediated photocatalysis treatment has a significant advantage to eliminate these contaminations in water [6]. In the presence of the photocatalyst, organic contaminants are directly oxidized by photogenerated holes and degraded into carbon dioxide and water to achieve degradation and purification. At the same time, the photocatalytic material itself has no loss.

As one of the important II-VI wide bandgap semiconductor materials, Zinc oxide (ZnO) has outstanding physical and chemical properties, such as high chemical stability, excellent electrochemical coupling coefficient, low cost and good biocompatibility [7]. It is considered a potential catalyst with good photodegradation activity for the degradation of organic pollutants in wastewater [8]. However, the rapid recombination rate of photogenerated electron-hole pairs and narrow light response range (only active under UV light) limit its wide applications [9]. Many researches have been done to enhance the photocatalytic activity of zinc oxide, especially to change the structure of zinc oxide as a facile and high-efficiency method. The structure of zinc oxide exists in the form of one-dimensional (1D), two-dimensional (2D) and three-dimensional (3D) structures [10,11]. The one-dimensional structure has various appearances such as nanorods, needles, spirals, wires, tubes, and combs [12]. The two-dimensional structure of zinc oxide includes nanosheets and nanolayers [13]. The three-dimensional structure of zinc oxide mainly manifests as flower-like, dandelion and snowflake [14]. Many physical characteristics of ZnO nanoparticles, such as the morphology and size, can be finely controlled by different synthesis methods, which have greatly influenced their properties [15]. In the synthesis process of nanomaterials, introducing a template is usually used to control the morphology and structure, and the controllable synthesis of the material is realized by the structure inducing effect.

Ionic liquids (ILs) are salts composed of an organic cation and an inorganic or organic anion. They possess excellent physical and chemical properties such as low melting point, negligible vapor pressure, mild reaction conditions and high thermal stability [16,17]. Ionic liquids can self-assemble into micelles in aqueous solvents and be used as templates to prepare nanostructured materials. The nanoparticles tend to aggregate and form a specific spatial morphology around these micelles, which functions like surfactants [9]. Du et al. [18] produced a yolk-shell silica sphere consisting of a core and an outer shell by a one-step process using a trisiloxane-tailed surface active ionic liquid as a template, the particle size and shell thickness improved with the increased ILs concentration. Thus, ILs are

†To whom correspondence should be addressed.
E-mail: shktang@tju.edu.cn
‡This author contributed equally to this work.

ideal templates for preparing ZnO materials with peculiar structures and unique properties [19,20].

Supramolecular gel is an essential kind of soft material, possessing a 3D network assembled from low-molecular-weight gels [21, 22]. Since Shinkai first reported the supramolecular gels in 1998, this soft material has had numerous potential applications in catalysis [23], optoelectronics [24], biomedicine [25] and sensors [26] owing to its unique properties. During the formation of supramolecular gels, gelation occurs through intermolecular non-covalent interactions, including hydrogen bonding, π-π stacking, van der Waals forces and dipole and electrostatic interactions, thereby resulting in the formation of various nanoscale structures such as fibrils, spirals, ribbons, tubes, layers [27,28]. The diversity of gel microstructures allows them to be utilized as templates to construct novel nanostructures and functional materials, adjusting the shape and size of nanomaterials such as silicon dioxide [29], titanium dioxide [30], gold and silver [31]. For example, Cui et al. [32] synthesized γ-Al_2O_3 with a worm-like mesoporous structure and high specific surface area in GP-1/propylene glycol gel. However, to our best knowledge, work on regulating the morphology of ZnO co-templated by ionic liquids and supramolecular gels has rarely been reported.

In this work, to overcome the complex reaction steps and harsh synthesis conditions as well high cost in the conventional synthesis methods of nano-ZnO, a control strategy using ionic liquids and supramolecular gels as co-template is proposed to control the crystal growth and morphology. ZnO crystals with a series of novel morphologies, including 2D nanosheets, 3D hydrangea flower-like and 3D hexagonal pencil clusters, have been systematically and successfully fabricated using the co-template method, fully presenting the role of the co-template in morphology control. The effects of co-template and the aging time on the morphology and structure of the synthesized zinc oxide are investigated. Furthermore, we present the microscopic mechanism of the synthesis of zinc oxide *via* the co-template method. When used as photocatalysts for degradation of Congo red solution under simulated solar light irradiation, the as-synthesized zinc oxide products with different morphologies exhibit enhanced photocatalytic activity and good recycling performance. This co-template method provides us a compelling synthesis of materials with novel morphologies.

EXPERIMENTAL SECTION

1. Materials

Tetramethyl ammonium glycinate ($[N_{1111}][Gly]$) was purchased from Lanzhou Institute of Chemical Physics (Lanzhou, China). *N*-lauroyl-*L*-glutamic acid di-n-butylamide (GP-1) was bought from Kishi-moto Sangyo Asia (Tokyo, Japan). $Zn(OAc)_2{\cdot}2H_2O$ was produced by Tianjin Yuanli Chemical Industry (Tianjin, China). Absolute ethanol and Congo red were purchased from Tianjin Jiangtian Chemical Technology Limited Company (Tianjin, China). All chemicals were analytic reagents and used directly without any pretreatment. The molecular structures of GP-1 and $[N_{1111}][Gly]$ are shown below in Scheme 1.

2. Synthesis of ZnO within $[N_{1111}][Gly]$/GP-1 Co-template

In this study, zinc oxide was synthesized with an amino acid ionic liquid $[N_{1111}][Gly]$ and an organic supramolecular gelator GP-1 as co-template *via* solvothermal method. In a typical procedure, 2.08 g $Zn(OAc)_2{\cdot}2H_2O$ and a certain amount of $[N_{1111}][Gly]$ were dissolved in 50 mL absolute ethanol-deionized water solution with the molar ratio of 0.2 under stirring for 15 min at room temperature. And 4 M NaOH was added to the solution at a 1 mL/min rate under stirring until pH=12. Then, 0.83 g GP-1 was added to the above-obtained solution, stirred until dissolved. The obtained solution was transferred into a 100 mL stainless steel autoclave and heat-treated at 140 °C for a certain time. After being finished, it was taken out and cooled to room temperature. The reaction mixture was centrifuged, washed with absolute ethanol and deionized water several times, and dried at 60 °C under vacuum for 24 h to obtain the white powder. Here the final samples are abbreviated as MZ-*x*-*t*, where *x* represents the molar ratio of $[N_{1111}][Gly]$ to $Zn(OAc)_2{\cdot}2H_2O$, *t* represents the aging time (h).

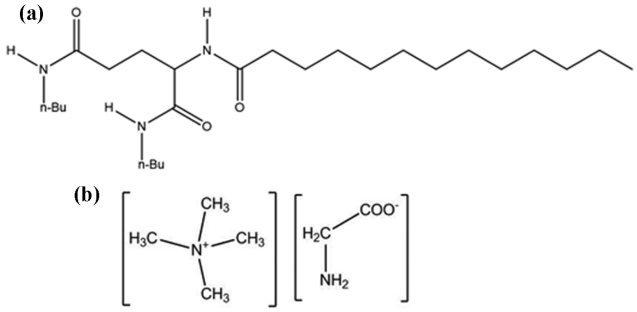

Scheme 1. Molecular structures of (a) *N*-lauroyl-*L*-glutamic acid di-n-butylamide and (GP-1) and (b) Tetramethyl ammonium glycinate ($[N_{1111}][Gly]$).

3. Degradation of Congo Red with the Synthesized ZnO as Photocatalyst

The degradation of Congo red took place in a beaker under simulated solar light (300 W) at room temperature. In a typical run, 50 mg synthesized ZnO samples were dispersed into 100 mL of Congo red aqueous solution with a concentration of 50 mg/L. Before irradiation, the solution was stirred in dark conditions for 60 min to reach an adsorption-desorption equilibrium. Next, 3 mL reaction solution was taken out at intervals of 15 min and then centrifuged at 10,000 rpm for 5 min. Dye concentration was analyzed by UV-vis spectrophotometer at λ_{max}=498 nm.

4. Characterization

N_2 adsorption and desorption isotherms were measured at 77 K by an ASAP analyzer (Tristar 3000, Micromeritics, USA). X-ray powder diffraction (XRD) recorded the crystalline phase compositions and crystallinity of ZnO on an X'Pert Pro diffractometer with a Cu Kα radiation source (λ=1.54056 Å). The particle morphology was observed by a JEM-2100F transmission electron microscope (Japan). The microstructure of samples was characterized by an S-4800 field emission scanning electron microscope (Hitachi, Japan) with an accelerating voltage of 0.1-30 KV. The UV-vis diffuse reflectance spectrums were obtained using a Shimadzu UV-2550 spectrophotometer. Photoluminescence (PL) spectra were obtained with a Xe lamp as the excitation light source at room temperature using an FLS1000 fluorescent spectrometer (Edinburgh).

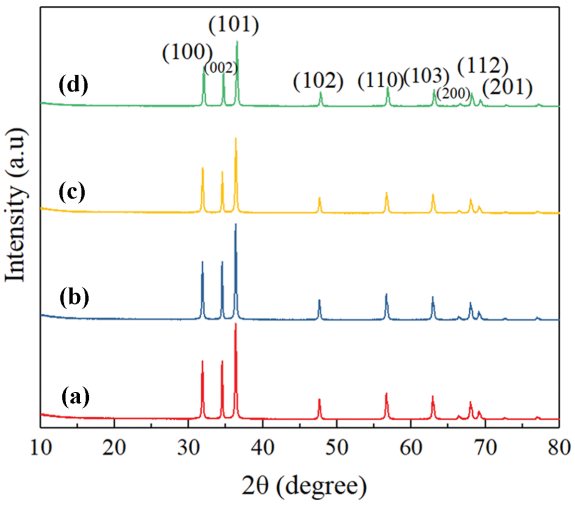

Fig. 1. XRD patterns of samples synthesized at different dosages of $[N_{1111}][Gly]$: (a) MZ-0.5-24, (b) MZ-1-24, (c) MZ-2-24, (d) MZ-3-24.

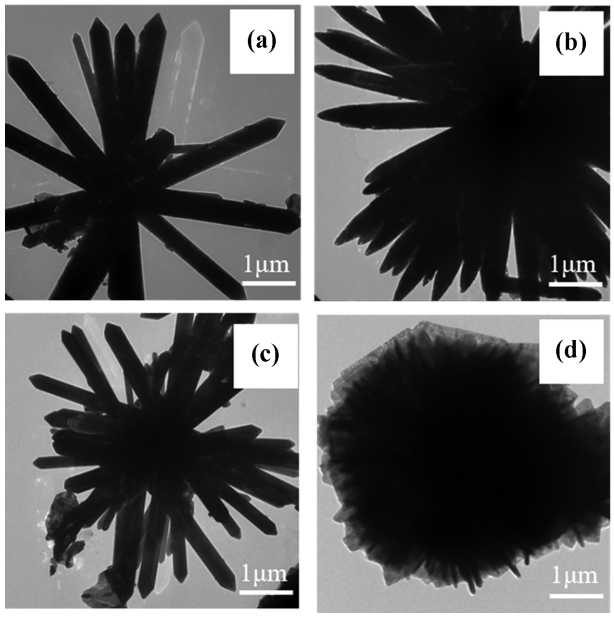

Fig. 3. Typical TEM images of ZnO synthesized at different dosages of $[N_{1111}][Gly]$: (a) MZ-0.5-24, (b) MZ-1-24, (c) MZ-2-24, (d) MZ-3-24.

RESULTS AND DISCUSSION

1. Effect of the amount of Ionic Liquids

The molar ratio of $[N_{1111}][Gly]$ to the zinc source increased from 0.5 to 3 while the aging time was uniformly set at 24 h. Fig. 1 shows the XRD pattern of zinc oxide samples synthesized with increased $[N_{1111}][Gly]$ dosages. All the samples have prominent diffraction peaks around 31.8°, 34.6°, 36.2°, 47.5°, 56.5°, 62.7°, 66.2°, 67.8° and 69.1° assigned to (100), (002), (101), (102), (110), (103), (200) and (201) characteristic peaks, respectively. Compared with the standard diffraction pattern, it can be indexed to hexagonal wurtzite ZnO structure (JCPDS: 36-1451). Besides, no other diffraction peaks are observed, revealing the high purity of the product. For all samples, the narrow full width-half maximum (FWHM) of (100), (002) and (101) diffraction peaks indicates that the crystallinity is relatively high. Additionally, the intensity of the diffraction peak gradually decreases with the increase of ionic liquid $[N_{1111}][Gly]$. Based on the above analysis, ZnO particles with higher purity and good crystallinity can be synthesized using $[N_{1111}][Gly]$ and GP-1 co-template.

To figure out the effect of co-template on the microstructure of zinc oxide products, SEM and TEM observations were carried out on samples synthesized with the increased $[N_{1111}][Gly]$ dosages. It

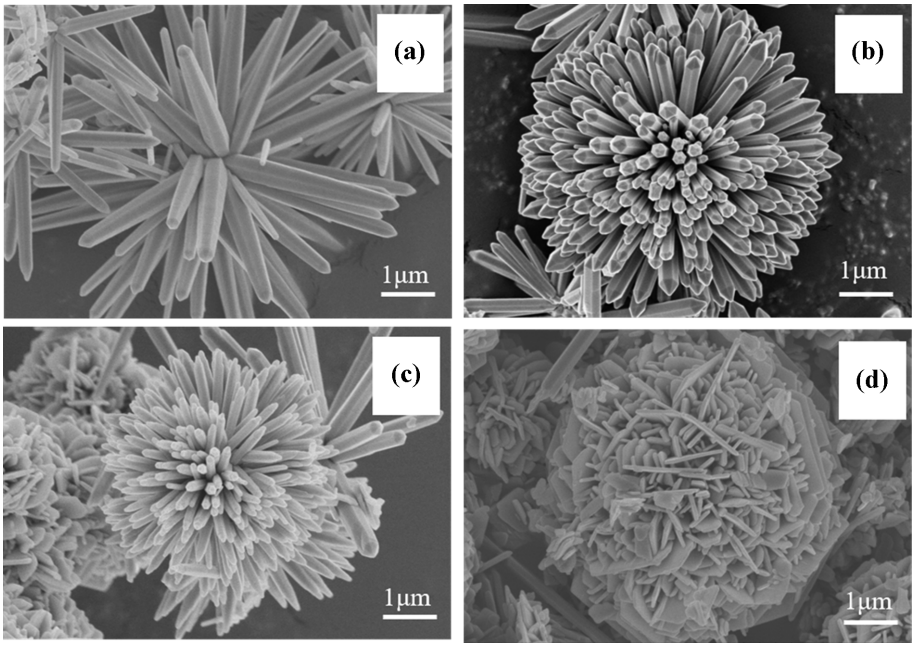

Fig. 2. Typical SEM images of ZnO synthesized at different dosages of $[N_{1111}][Gly]$: (a) MZ-0.5-24, (b) MZ-1-24, (c) MZ-2-24, (d) MZ-3-24.

is clear that the morphology of the synthesized products varies with the amount of ionic liquid. When the amount of $[N_{1111}][Gly]$ is low (Fig. 2(a), 3(a)), the products tend to exhibit a hexagonal pencil cluster structure with a uniform thickness from the flower core to the tail end. Increasing the molar ratio of $[N_{1111}][Gly]$ to zinc source to 1.0 (Fig. 2(b), 3(b)), the hexagonal pencil clusters are evenly distributed in all directions and become denser. Obviously, the tail ends are hexagonal pyramids, wherein the hexagonal prisms have a length of 3-5 μm and a radial dimension of 200-300 nm. A small number of polygonal nanosheets appear when the molar ratio of $[N_{1111}][Gly]$ to the zinc source reaches 2.0 (Fig. 2(c), 3(c)), and the obtained products show a pencil cluster structure with some polygonal nanosheets on the surface. When the molar ratio of $[N_{1111}][Gly]$ to zinc source rises to 3.0 (Fig. 2(d), 3(d)), the products exhibit hydrangea flower morphology assembled from polygonal nanosheets with a diameter of about 5 μm. In summary, the amount of ionic liquid $[N_{1111}][Gly]$ has a significant effect on the microstructure of the product. By adjusting the ratio of $[N_{1111}][Gly]$ in the co-template, the morphology of zinc oxide can be transformed between hexagonal pencil cluster and hydrangea flower assembled with polygonal nanosheets.

2. Effect of the Aging Time

Based on the previous experiments, the effect of the aging time was studied with the molar ratio of $[N_{1111}][Gly]$ to zinc source kept at 3.0. Fig. 4 shows the SEM images of zinc oxide products obtained at different aging time. As depicted in Fig. 4(A), the product is

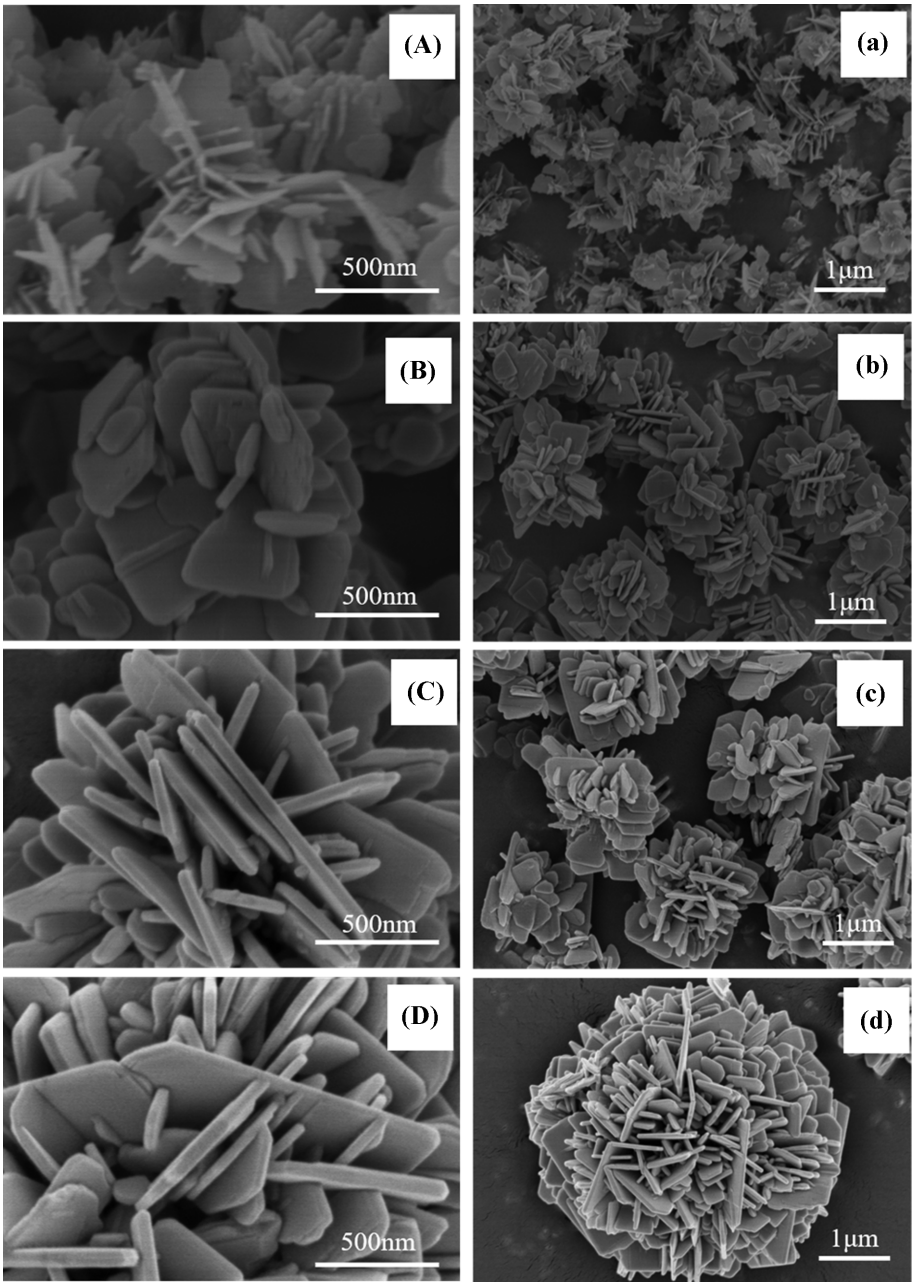

Fig. 4. Typical SEM images of ZnO synthesized at different aging time: (A), (a) MZ-3-8, (B), (b) MZ-3-12, (C), (c) MZ-3-18, (D), (d) MZ-3-24.

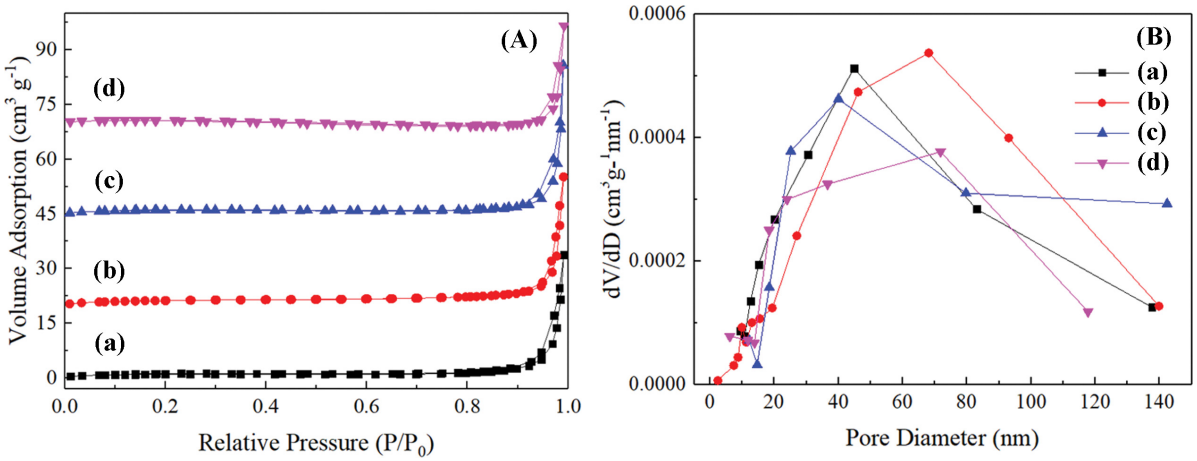

Fig. 5. N_2 adsorption/desorption isotherms (A) and pore size distributions (B) of ZnO synthesized. (a) MZ-3-8, (b) MZ-3-12, (c) MZ-3-18, (d) MZ-3-24.

cluster-stacked with a plurality of irregular sheets when the aging time is 8 h. As the reaction time is prolonged, the sheets begin to appear angular shaped (Fig. 4(B), (b)) and the clusters are more densely packed. When the aging time is 24 h, the product is structurally completed and shows regular morphology of hydrangea flower assembled with nanosheets (Fig. 4(D), (d)). The degree of nucleation growth changes with the aging time, leading to the diversity of ZnO morphology. Thus, the results demonstrate the aging time has a great influence on the morphology of the sample.

Fig. 5 shows the N_2 isothermal adsorption-desorption curves of the zinc oxide products obtained at different aging time and the corresponding pore size distribution curves. The effects of the aging time on the surface area and the pore structure of the product are further studied. Obviously, all the curves show the characteristics of type IV isotherms, suggesting that the synthesized zinc oxide has a distinct mesoporous structure, and a typical H4 type hysteresis loop is observed in the higher relative pressure region, corresponding to the slit hole passage formed by the layered structure stacking. All products have wide pore size distribution (2-140 nm),

Table 1. Pore parameters of the products synthesized ZnO at different aging time

Sample	S_{BET} (m^2/g)	D_{pore} (nm)	V_{pore} (cm^3/g)
MZ-3-8	4.82	48.73	0.05
MZ-3-12	3.92	52.72	0.05
MZ-3-18	3.85	62.19	0.06
MZ-3-24	2.34	67.07	0.04

the pore structure is irregular and there are a number of large pores attributed to the free accumulation of zinc oxide flakes. With the increase of the aging time, the size of the nanosheet gradually expands, the specific surface area (Table 1) is slightly reduced, and the average pore diameter gradually becomes more immense. In particular, the aging time has no significant effect on the pore volume of the product.

3. Mechanism of ZnO Synthesis within the Co-template

Based on the above results, we propose the growth and formation mechanism of the co-template-induced synthesis of hexagonal

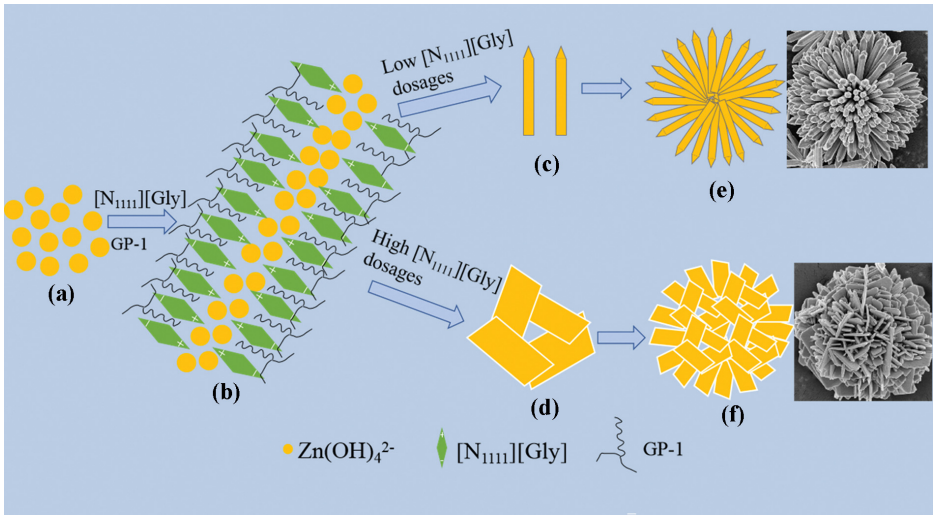

Fig. 6. Schematic mechanism of the formation of ZnO with co-template.

pencil clusters and hydrangea flower-like zinc oxide. When zinc source slowly dissociates in sodium hydroxide solution (pH=12), the Zn^{2+} primarily forms $Zn(OH)_4^{2-}$ initial grains (Fig. 6(a)) combined with OH^- by hydrolysis. The chemical reaction can be formulated as [33,34]:

$$Zn(CH_3COO)_2 + NaOH \rightarrow Zn(OH)_4^{2-}$$

After the ionic liquid is added to the system, the cation of the ionic liquid can be stably adsorbed on the surface of the negatively charged $Zn(OH)_4^{2-}$ grain to form $[N_{1111}][Gly]$-Zn-OH complex. The ionic liquid can affect the growth rate of the crystal *via* hydrogen bonding-co-π-π interaction, and induce the preferential growth of the ZnO nucleus in a certain direction, which plays the role of the soft template. GP-1 self-assembles to form fiber structure, the $[N_{1111}][Gly]$-Zn-OH complex is arranged along the surface of the GP-1 fiber under strong intermolecular hydrogen bonding (Fig. 6(b)). When the proportion of $[N_{1111}][Gly]$ in the co-template is relatively low, the ZnO nanocrystals are arranged along the long and dense GP-1 fibers and preferentially grow to form hexagonal pencil-shaped zinc oxide (Fig. 6(c)). When the ratio of $[N_{1111}][Gly]$ is relatively high, GP-1 fibers are shorter and more dispersed. Meanwhile, more $Zn(OH)_4^{2-}$ adsorb $[N_{1111}][Gly]$ to form polygonal flakes of zinc oxide (Fig. 6(d)). Then zinc oxide begins to self-assemble with Oswald ripening. As ZnO crystals radially grow layer by layer, hexagonal nanopencils or nanosheets that are growing or have stopped growing on the outside will limit the growth of the inner nanocrystals to some extent, and the distance between the crystals gradually shrinks. Eventually, a hexagonal pencil cluster (Fig. 6(e)) or hydrangea flower-like zinc oxide (Fig. 6(f)) with regular morphology is formed. Ionic liquid-supramolecular gel as co-template induces the synthesis of ZnO nanomaterials, and plays an important role in inducing ZnO crystal orientation growth and constructing final morphology [35,36].

4. Optical Properties of ZnO with Different Morphologies

Fig. 7 shows UV-vis DRS absorption spectra (a) and Tauc's plot (b) of ZnO with different morphologies. The band gap energy (E_g) is calculated by the following formula [37,38]:

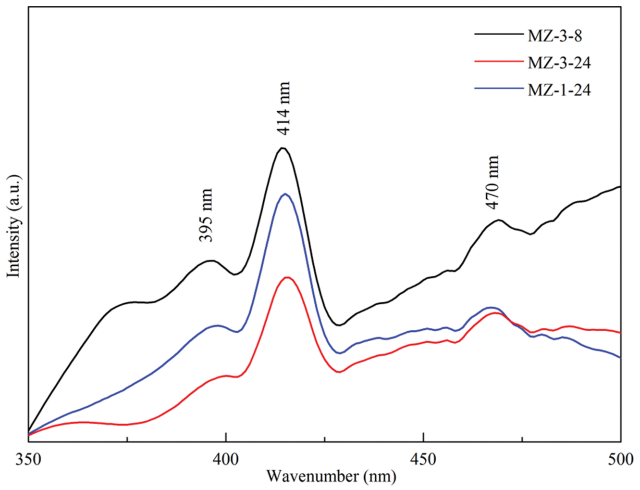

Fig. 8. PL spectra of ZnO with different morphologies.

$$\alpha h\nu = A(h\nu - E_g)^{n/2} \quad (1)$$

where α is the absorbance, $h\nu$ is photon energy, h is Planck's constant, A is the proportion constant, n is assumed to be 1 and E_g is the band gap. The calculated band gap values of MZ-3-8, MZ-3-24 and MZ-1-24 are 3.16 eV, 3.21 eV and 3.22 eV, respectively. These results are in good agreement with the value reported in other literature [39]. Compared with MZ-3-24 and MZ-1-24, the absorption edge of MZ-3-8 gradually shifts to the distribution wavelength in the visible region, and the optical band gap decreases, which means that the photocatalytic performance of MZ-3-8 is enhanced.

Fig. 8 shows PL spectra of the ZnO with different morphologies. It is clear that the spectra of the ZnO with different morphologies are similar. A violet-blue emission band at about 395 nm and 414 nm, and a blue-green emission at about 470 nm are observed [40,41]. It can also be seen from Fig. 8 that the emission intensity for MZ-3-8 is higher than that of MZ-3-24 and MZ-1-24. The improvement of the PL intensity of MZ-3-8 is due to the increase

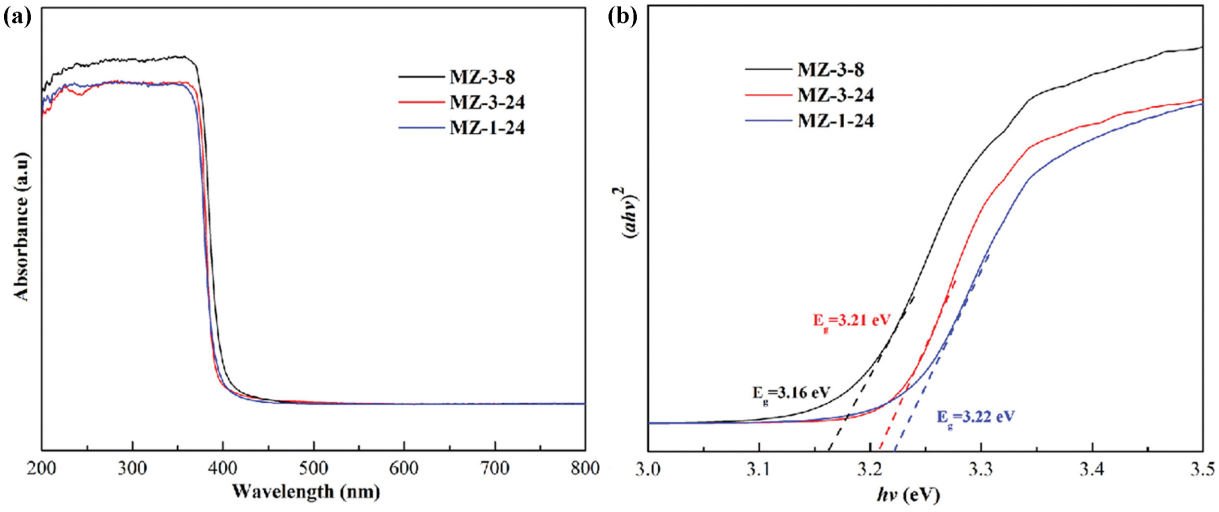

Fig. 7. UV-vis DRS absorption spectra (a) and Tauc's plot (b) of ZnO with different morphologies.

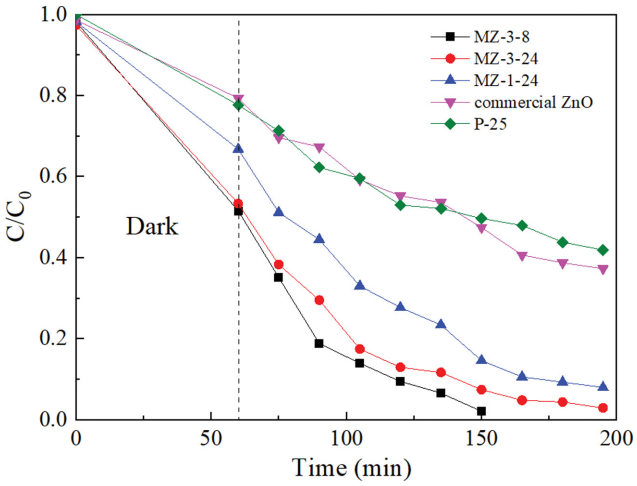

Fig. 9. Degradation of Congo Red catalyzed by ZnO with different morphologies and P25.

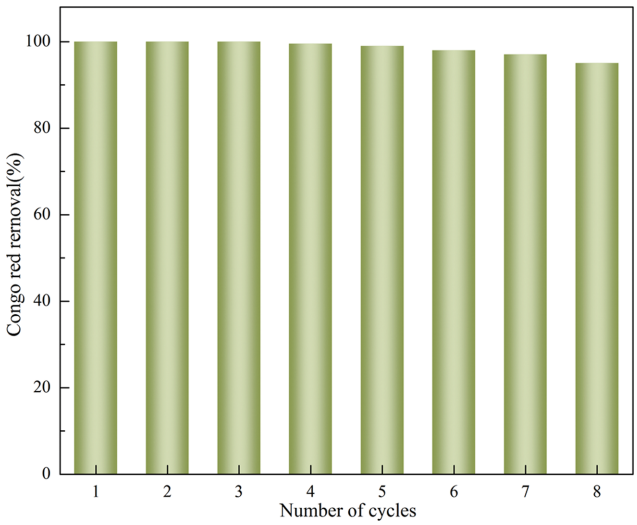

Fig. 10. Cyclic performance of ZnO (Sample MZ-3-8) in the degradation of Congo Red: ([Congo red]=50 mg/L, [ZnO]=0.5 g/L).

of oxygen vacancy and/or crystal defect, which is in favor of photocatalytic reaction [42,43].

5. Photocatalytic Behavior

The photocatalytic activity of as-fabricated ZnO products was evaluated by the degradation of Congo red solution under simulated solar light irradiation. Fig. 9 shows the simulated solar light degradation activity of MZ-3-8, MZ-3-24, MZ-1-24, commercial ZnO and P-25. Samples MZ-3-8, MZ-3-24 and MZ-1-24 correspond to nanosheets, hydrangea flower-like and hexagonal pencil clustered zinc oxide, respectively. It is clear that all the samples reach an adsorption-desorption equilibrium when the irradiation time is 60 min (Fig. 9). The result demonstrates that all ZnO materials prepared by ionic liquid-supramolecular gel co-template exhibit excellent catalytic performance under simulated solar light irradiation, obviously superior to commercial zinc oxide and P-25 (Table 2). Indeed, MZ-3-8 exhibits comparable Congo red degradation performance in contrast to that of most reported ZnO composites. Among them, zinc oxide nanosheets (sample MZ-3-8) are found to be the most active in the degradation, evidenced by the fact that the degradation rate reaches 98% for 90 min. However, the degradation rate of the commercially ZnO and P-25 degradation rate is only about 50% in the same condition. In addition, Fig. S1 demonstrates the degradation performance of MZ-3-12 and MZ-3-18 on Congo red under simulated solar light. Both MZ-3-12 and MZ-3-18 show modest degradation rates of 97% at the same amount of catalysts compared with MZ-3-8 and MZ-3-24.

It is known that the photocatalytic redox reaction mainly takes place on the surface of the photocatalysts. The photocatalytic efficiency is closely related to the absorption intensity in the visible and near-ultraviolet light region. Since the ZnO nanosheets (sample MZ-3-8) have the smallest particle size, more electron holes are generated under irradiation with the increased absorption area. The electron holes migrate to the surface of ZnO nanosheets and then form hydroxyl radicals, adsorbing more anionic dye Congo red onto the surface of the photocatalyst, resulting in the enhancement of the degradation rate. Photocatalytic mechanism for the degradation of Congo red is presented in Fig. S2.

6. Reusability of ZnO Catalysts

To consider the chemical stability and reproducibility of the catalyst is of great significance in its practical application. The stability and reusability of the prepared ZnO catalyst for Congo red degradation under simulated solar light irradiation were investigated. MZ-3-8 was selected as the sample for the reusability experiment. As displayed in Fig. 10, MZ-3-8 shows the best catalytic performance

Table 2. Degradation of Congo red catalyzed by the prepared samples and other reported ZnO materials

Sample	C_0 (mg/L)	m (mg)	t (min)	Degradation rate	Reference
MZ-3-8	50	50	90	98%	This work
MZ-3-24	50	50	135	96%	This work
MZ-1-24	50	50	135	92%	This work
ZnO	50	50	40	22%	[44]
ZnO/Zeolite	10	200	60	97.16%	[45]
ZnO/rGO	10	200	60	97.96%	[46]
ZnO/ZrO_2/MMT	10	50	30	92%	[47]
PAn/ZnO	50	100	30	67%	[48]
P-25	50	50	135	54%	This work

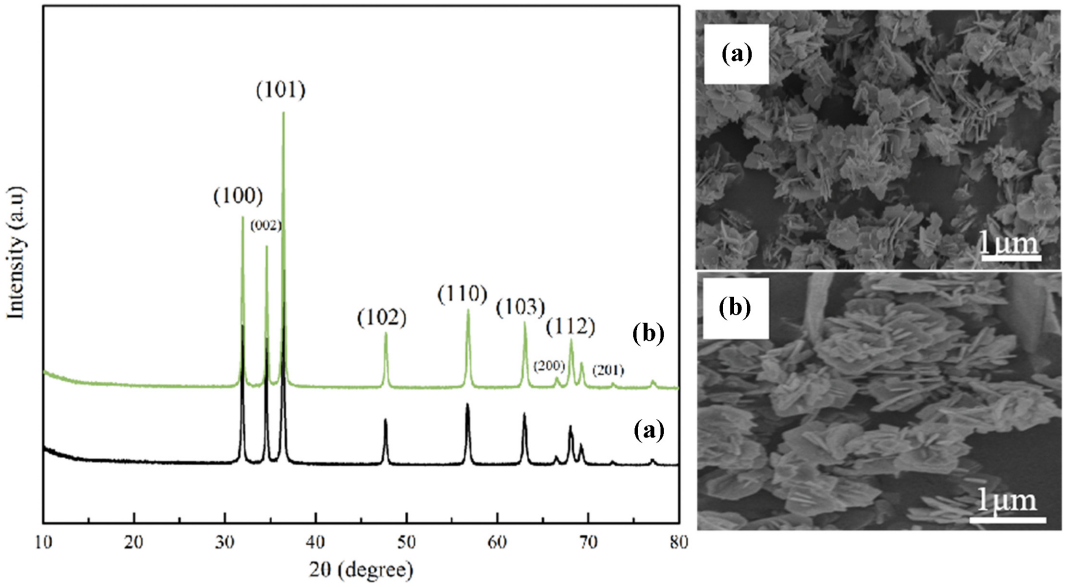

Fig. 11. XRD patterns and SEM images of ZnO (a) MZ-3-8, (b) eight recycling experiments of MZ-3-8 for Congo red degradation.

with a degradation rate near 100%. The degradation rate of Congo red remains at about 95%, and the degradation rate does not decrease significantly after eight cycles. The remarkable results indicate that MZ-3-8 possesses good catalytic stability. XRD and SEM were used to characterize MZ-3-8 after the reusability test. As shown in Fig. 11, the crystal structure of MZ-3-8 remains unchanged after recycling experiments and there is no significant change in the morphology between the eighth reused sample and the fresh one.

CONCLUSIONS

We developed a facile, mild, and versatile strategy to synthesize zinc oxide with specific morphology. For the first time, hydrangea flower-like and hexagonal pencil-clustered zinc oxide were synthesized using $[N_{1111}][Gly]$ and GP-1 as the co-template. $[N_{1111}][Gly]$ can affect the growth rate of the crystals *via* H-bonding-co-p-p interaction and induce the preferential growth of the ZnO nucleus in a certain direction. GP-1 molecules self-assemble to form a fiber network structure, and $[N_{1111}][Gly]$-Zn-OH complexes are arranged along the surface of GP-1 fibers with strong intermolecular hydrogen bonding. Additionally, ZnO with different morphology has an effect on photocatalytic activity. MZ-3-8 with nanosheets morphology displays excellent catalytic performance with a degradation rate near 100% for 90 min, obviously superior to commercial ZnO and P-25. Furthermore, the catalyst can be reused several times with a slight loss of photocatalytic activity. The catalyst possesses wide application prospects in the fields of photocatalysis and environmental protection.

SUPPORTING INFORMATION

Additional information as noted in the text. This information is available via the Internet at http://www.springer.com/chemistry/journal/11814.

REFERENCES

1. K. M. Lee, C. W. Lai, K. S. Ngai and J. C. Juan, *Water Res.*, **88** 428 (2016).
2. Q. Sun, M. Tang, P. V. Hendriksen and B. Chen, *J. Alloy. Compd.*, **829**, 154552 (2020).
3. H. Guo, Z. Yu, Y. Su and X. Jiang, *Inorg. Chim. Acta*, **508**, 119625 (2020).
4. X. Huang, Y. Wan, B. Shi, J. Shi, H. Chen and H. Liang, *Chemosphere*, **249**, 126129 (2020).
5. D. Yuan, C. Zhang, S. Tang, X. Li, J. Tang, Y. Rao, Z. Wang and Q. Zhang, *Water Res.*, **163**, 114861 (2019).
6. J. Sin and S. Lam, *Mater. Lett.*, **182**, 223 (2016).
7. L. Chen, *Adv. Mat. Res.*, **1** (2013).
8. C. Sushma and S. G. Kumar, *Chem. Pap.*, **71**, 2023 (2017).
9. S. Zhao, Y. Zhang, Y. Zhou, C. Zhang, J. Fang and X. Sheng, *Appl. Surf. Sci.*, **410**, 334 (2017).
10. P. Basnet, T. I. Chanu, D. Samanta and S. Chatterjee, *J. Photoch. Photobio. B.*, **183**, 201 (2018).
11. R. Kumar, O. Al-Dossary, G. Kumar and A. Umar, *Nano-Micro Let.*, **7**, 97 (2015).
12. S. Lam, J. Sin, A. Z. Abdullah and A. R. Mohamed, *Sep. Purif. Technol.*, **132**, 378 (2014).
13. M. Perez-Page, E. Yu, J. Li, M. Rahman, D. M. Dryden, R. Vidu and P. Stroeve, *Adv. Colloid Interface*, **234**, 51 (2016).
14. M. Movahedi, A. R. Mahjoub, I. Yavari and E. Kowsari, *J. Nanosci. Nanotechno.*, **10**, 6173 (2010).
15. S. R. Saptarshi, A. Duschl and A. L. Lopata, *Nanomedicine-UK*, **10** (2015).
16. R. Martínez-Palou, *Mol. Divers.*, **14**, 3 (2010).
17. W. Zheng, D. Li and W. Guo, *Ionic liquids-current state of the art*, Intech: Croatia (2015).
18. Z. Du, E. Li, G. Li, F. Cheng and G. Wang, *J. Mater. Sci.*, **49**, 4919 (2014).
19. R. Ramanathan, J. L. Campbell, S. K. Soni, S. K. Bhargava, V. Ban-

sal and M. Antopolsky, *PLoS One*, **6**, 17707 (2011).
20. S. Sarkar, K. Mantri, D. Kumar, S. K. Bhargava and S. K. Soni, *RSC Adv.*, **5**, 105800 (2015).
21. G. Yu, X. Yan, C. Han and F. Huang, *Chem. Soc. Rev.*, **42**, 6697 (2013).
22. T. Kajita, A. Noro and Y. Matsushita, *Polymer*, **128**, 297 (2017).
23. J. Zhu, R. Wang, R. Geng, X. Zhang, F. Wang, T. Jiao, J. Yang, Z. Bai and Q. Peng, *RSC Adv.*, **9**, 22551 (2019).
24. K. Rao, M. Hossain and B. Umesh, *J. Org. Chem.*, **91** (2013)
25. M. E. Roth-Konforti, M. Comune, M. Halperin-Sternfeld, I. Grigoriants, D. Shabat and L. Adler-Abramovich, *Macromol. Rapid Comm.*, **39**, 1800588 (2018).
26. M. S. de Luna, V. Marturano, M. Manganelli, C. Santillo, V. Ambrogi, G. Filippone and P. Cerruti, *J. Colloid Interface Sci.*, **568**, 16 (2020).
27. K. Y. Kim, M. Ok, J. Kim, S. H. Jung, M. L. Seo and J. H. Jung, *GELS*, **6**, 16 (2020).
28. V. C. Edelsztein, C. A. Mac, M. Ciarlantini and P. H. Di Chenna, Beilstein, *J. Org. Chem.*, **9**, 1826 (2013).
29. N. Saito and M. Yamaguchi, *Molecules*, **23**, 277 (2018).
30. Y. He and Y. Yang, *Chem. Rec.*, **17**, 1146 (2017).
31. G. Li, M. Liu, C. Song and Z. Yuan, *Appl. Surf. Sci.*, **493**, 94 (2019).
32. X. Cui, S. Tang and H. Zhou, *Mater. Lett.*, **98**, 116 (2013).
33. S. Bian, I. A. Mudunkotuwa, T. Rupasinghe and V. H. Grassian, *Langmuir*, **27**, 6059 (2011).
34. J. Han, W. Qiu and W. Gao, *J. Hazard. Mater.*, **178**, 115 (2010).
35. Y. J. Sun, L. Wang, X. G. Yu and K. Z. Cheng, *CrystEngComm*, **14**, 3199 (2012).
36. S. Kuriakose, N. Bhardwaj, J. Singh, B. Satpati and S. Mohapatra, *Beilstein J. Nanotech.*, **4**, 763 (2013).
37. N.Yusoff, S. VijayKumar, A. Pandikumar, N. M. Huang, A. R. Marlinda and M. N. An'amt, *Ceram. Int.*, **41**, 5117 (2015).
38. J. Yoon and S. G. Oh, *J. Ind. Eng. Chem.*, **96**, 390 (2021).
39. Q. Feng, S. Li, W. Ma, H. Fan, X. Wan, Y. Lei, Z. Chen, J. Yang and B. Qin, *J. Alloys Compd.*, **737** (2018).
40. I. Ahmad, S. Shukrullah, M. Ahmad, E. Ahmed, M. Y. Naz, M. S. Akhtar, N. R. Khalid, A. Hussain and I. Hussain, *Mater. Sci. Semicond. Process*, **123**, 105584 (2021).
41. I. Ahmad, S. Shukrullah, M. Y. Naz, H. N. Bhatti, M. Ahmad, E. Ahmed, S. Ullah and M. Hussien, *JECE*, **10** (2022).
42. D. Papadaki, G. H. Mhlongo, D. E. Motaung, S. S. Nkosi, K. Panagiotaki, E. Christaki, M. N. Assimakopoulos, V. C. Papadimitriou, F. Rosei, G. Kiriakidis and S. S. Ray, *Acs Omega*, **4**, 16429 (2019).
43. G. H. Mhlongo, K. Shingange, Z. P. Tshabalala, B. P. Dhonge, F. A. Mahmoud, B. W. Mwakikunga and D. E.Motaung, *Appl. Surf. Sci.*, **390**, 804 (2016).
44. F. Farzaneh, Z. Asgharpour, F. Nouroozi and S. Haghshenas, *J. Clust. Sci.*, **28**, 1637 (2017).
45. Z. Rahmayeni and S. Y. Adril, *Orient. J. Che.*, **34**, 887 (2018)
46. Y. L. Pang, S. F. Tee, S. Lim, A. Z. Abdullah, H. C. Ong, C. Wu, W. C. Chong, A. W. Mohammad and E. Mahmoudi, *Water Treat.*, **108** (2018).
47. S. Aghabeygi, M. Modaresi-Tehrani and S. Ahmadi, *J. Electron. Mater.*, **50**, 2870 (2021).
48. S. Zor and B. Budak, *Turk. J. Chem.*, **44**, 486 (2020).

Supporting Information

Controllable synthesis of zinc oxide with ionic liquid and supramolecular gel as co-template for the degradation of organic dyes

Zhen Li[*,‡], Lili Sun[*,‡], Jie Zhang[*], and Shaokun Tang[*,,†]**

*Key Laboratory for Green Chemical Technology of Ministry of Education, School of Chemical Engineering & Technology, Tianjin University, Tianjin 300072, China

**Collaborative Innovation Center of Chemical Science and Engineering (Tianjin), Tianjin University, Tianjin 300072, China

(*Received 11 March 2022 • Revised 27 June 2022 • Accepted 7 July 2022*)

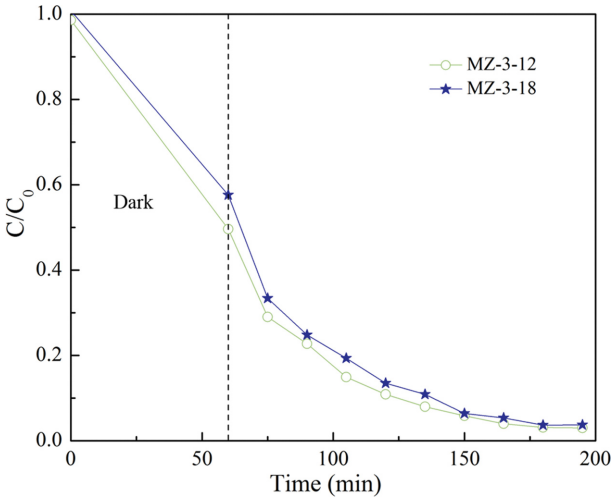

Fig. S1. Degradation of Congo red catalyzed by ZnO synthesized at different aging time.

Photocatalytic Degradation Mechanism of Congo Red Catalyzed by ZnO

Fig. S2 shows the photocatalysis mechanism of ZnO. ZnO is stimulated by simulated solar light irradiation, and a valence band electron (VB) transfers to the conduction band (CB), leaving a hole in the valence band (Eq. (1)). The electrons in ZnO conductivity band react with molecular oxygen to produce superoxide radical anion (Eq. (2)). The holes at ZnO valence band can oxidize adsorbed water or hydroxide ions to hydroxyl radicals (Eqs. (3) and (4)). The superoxide radical anion and hydroxyl radical are used for the

Table S1. Degradation of Congo red catalyzed by the prepared samples

Sample	C_0 (mg/L)	m (mg)	t (min)	Degradation rate
MZ-3-12	50	50	135	97%
MZ-3-18	50	50	135	97%

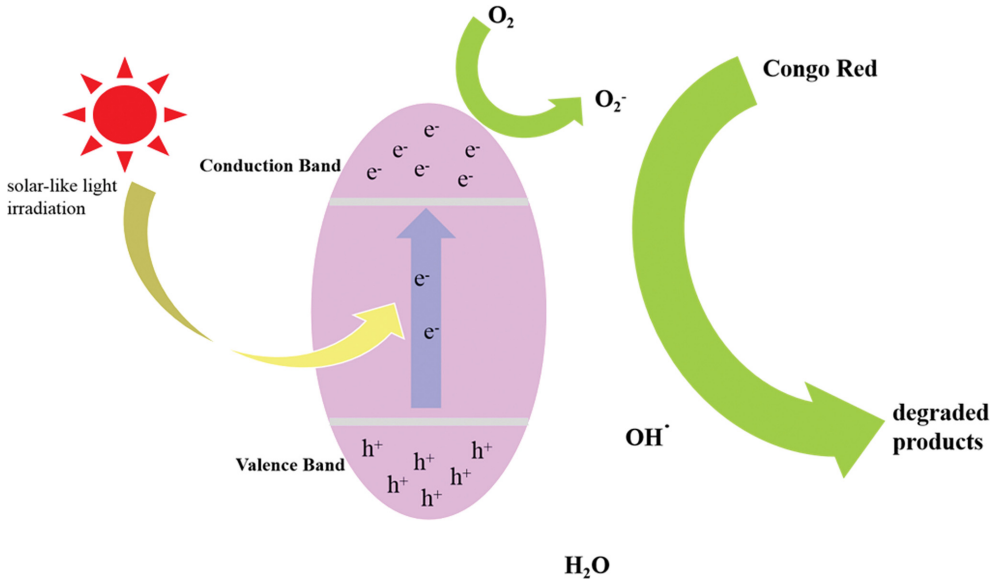

Fig. S2. Mechanism of photocatalytic degradation of Congo red by ZnO.

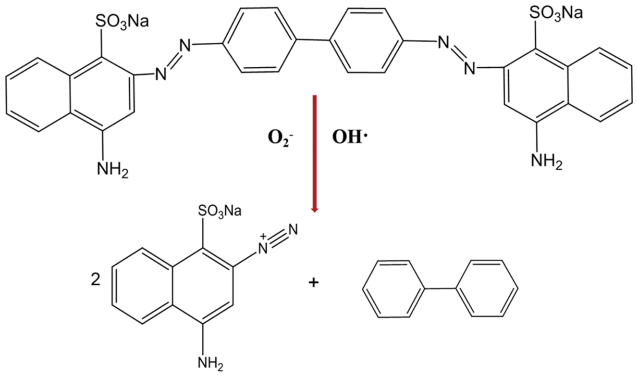

Fig. S3. Degradation of Congo red.

degradation of Cong red (Eq. (5)) [1,2].

$$ZnO + h\nu(\text{solar - like light}) \rightarrow e^-_{CB} + h^+_{VB} \quad (1)$$

$$e^-_{CB} + O_2 \rightarrow O_2^- \quad (2)$$

$$h^+_{VB} + H_2O \rightarrow H^+ + OH^- \quad (3)$$

$$h^+_{VB} + OH^- \rightarrow OH^\bullet \quad (4)$$

$$O_2^- + OH^\bullet + \text{Congo Red} \rightarrow \text{Degraded products} \quad (5)$$

According to the reported literatures [3-5], Congo red reacts with superoxide radical anion and hydroxide radical, and it is most likely that Congo red undergoes asymmetric cleavage to produce (4-amino-3-diazenylnaphthalene)-1-sodium sulfonate (2 molecules) and benzene (1 molecule) (Fig. S3). The intermediate product forms small molecule benzene derivatives by cleavage of the benzene ring, C single bond S bond from aromatic ring, C single bond N and C single bond C bond cleavage, N double bond N cleavage.

REFERENCES

1. L. Jing, Y. Qu, B. Wang. S. Li, B. Jiang, L. Yang, W. Fu, H. Fu and J. Sun, *Sol. Energy. Mater. Sol. Cells*., **90**, 1773 (2006).
2. M. Pera-Titus, V. G. Molina, M. A. Banos, J. Gimenz and S. Esplugas, *Appl. Catal. B Environ*., **47** (2004).
3. U. O. Bhagwat, J. J. Wu, A. M. Asiric and S. Anandan, *J. Photoch. Photobio. A*., **346** (2017).
4. U. O. Bhagwat, J. J. Wu, A. M. Asiri and S. Anandan, *Chemistryselect*., **3**, 788 (2018).
5. M. Thomas, G. A. Naikoo, M. U. D. Sheikh, M. Bano and F. Khan, *J. Photoch. Photobio. A*., **327** (2016).